



Aeromechanics Analysis of a Boundary Layer Ingesting Fan

Milind A. Bakhle¹

NASA Glenn Research Center, Cleveland, Ohio 44135, USA

T. S. R. Reddy²

University of Toledo, Ohio 43606, USA

Gregory P. Herrick³

NASA Glenn Research Center, Cleveland, Ohio 44135, USA

Aamir Shabbir⁴ and Razvan V. Florea⁵

United Technologies Research Center, East Hartford, Connecticut 06108

Boundary layer ingesting propulsion systems have the potential to significantly reduce fuel burn but these systems must overcome the challenges related to aeromechanics – fan flutter stability and forced response dynamic stresses. High-fidelity computational analysis of the fan aeromechanics is integral to the ongoing effort to design a boundary layer ingesting inlet and fan for fabrication and wind-tunnel test. A three-dimensional, time-accurate, Reynolds-averaged Navier Stokes computational fluid dynamics code is used to study aerothermodynamic and aeromechanical behavior of the fan in response to both clean and distorted inflows. The computational aeromechanics analyses performed in this study show an intermediate design iteration of the fan to be flutter-free at the design conditions analyzed with both clean and distorted in-flows. Dynamic stresses from forced response have been calculated for the design rotational speed. Additional work is ongoing to expand the analyses to off-design conditions, and for on-resonance conditions.

I. Introduction

Boundary layer ingestion (BLI) propulsion has the potential for significant reduction in aircraft fuel burn¹; previous system studies²⁻⁶ have shown that 5-10% reduction in fuel burn is possible. Recent work⁷ has confirmed this potential benefit through a system study focused on the propulsion system and its integration into the Blended Wing Body (BWB) aircraft. The system study indicated that low-loss inlets and high-performance, distortion-tolerant turbomachinery are key technologies required to achieve a 3-5% BLI fuel burn benefit for future aircraft relative to a baseline high-performance, pylon-mounted, propulsion system. The study further identified the key sensitivity parameters and their desired targets. However, this system-level benefit could be diminished by not achieving the targets of inlet total pressure loss, fan efficiency reduction, and fan stall margin reduction. Further, the fan must meet aeromechanics requirements regarding dynamic stresses and flutter stability. Efforts⁸ are currently in progress to design and fabricate the inlet and fan for a BLI propulsion system that will be tested in a wind-tunnel to simulate cruise conditions of a representative large commercial transport aircraft. This paper describes in detail a preliminary computational aeromechanics analysis performed on the boundary layer ingesting fan. The objectives of the aeromechanics analysis are to determine the dynamic stresses in the fan blade due to operation in a distorted inflow and to determine the flutter stability of the fan. The present aeromechanics analysis is performed at flight conditions and further studies are required at more challenging conditions including take-off.

The inlet duct that brings the flow to the fan face is very important element of this propulsion system. Under a separate effort, the NASA Inlet A⁹ has been used as the starting point for the design of the inlet used in the current

¹ Aerospace Engineer, Structures and Dynamics Branch, AIAA Associate Fellow.

² Senior Research Associate, Structures and Dynamics Branch, AIAA Associate Fellow.

³ Aerospace Engineer, Structures and Dynamics Branch, AIAA Member.

⁴ Research Engineer, Aerodynamics, currently at Pratt & Whitney, AIAA Member.

⁵ Research Engineer, Thermal & Fluid Sciences, AIAA Member.

study. An optimization-based parametric inlet design system was developed and applied to considerably reduce the total pressure loss and the distortion harmonic amplitudes⁸.

II. Fan Aerodynamic Analysis

Fan aerodynamic analysis in the present work is based on the time-domain solution of Reynolds-averaged Navier Stokes (RANS) equations using the TURBO aeroelastic analysis code^{10,11}. Briefly, this is an implicit finite-volume RANS solver that uses structured multi-block grids to model flow through one or more blade rows. Previous applications of TURBO in the study of flutter and forced vibration are presented in Refs. 12-14. Further validation of TURBO in the study of aeromechanics is available in Refs. 15-19. An inlet distortion boundary condition is used at the upstream boundary to prescribe the flow entering the fan domain since the inlet duct is not modeled in this part of the work. With this inlet distortion boundary condition, total conditions are held (at each respective radial and azimuthal location where prescribed) as governed by the characteristics; Herrick²⁰ implemented and applied this boundary condition in previous work. A throttle exit boundary condition is used at the downstream boundary to avoid over-constraining the exit flow; this boundary condition maintains only the integrated corrected mass flow through the exit plane at a prescribed value, while local flow quantities are free to attain local equilibrium. For fan aeromechanics analysis with blade vibrations, dynamic grid deformation is used to prescribe harmonic blade vibrations and the energy method is used to evaluate aerodynamic damping and flutter stability.

Since the design of the BLI fan is in progress, the analyses presented in this paper are performed on an aerodynamic design iteration. The computational meshes used in this study of the BLI fan include a combination of H, O, and C block meshes. Figure 1a shows the computational domain for the BLI fan (one blade passage); Fig. 1b shows the fan rotor blade and Fig. 1c shows a cross-sectional view at a fixed radial location.

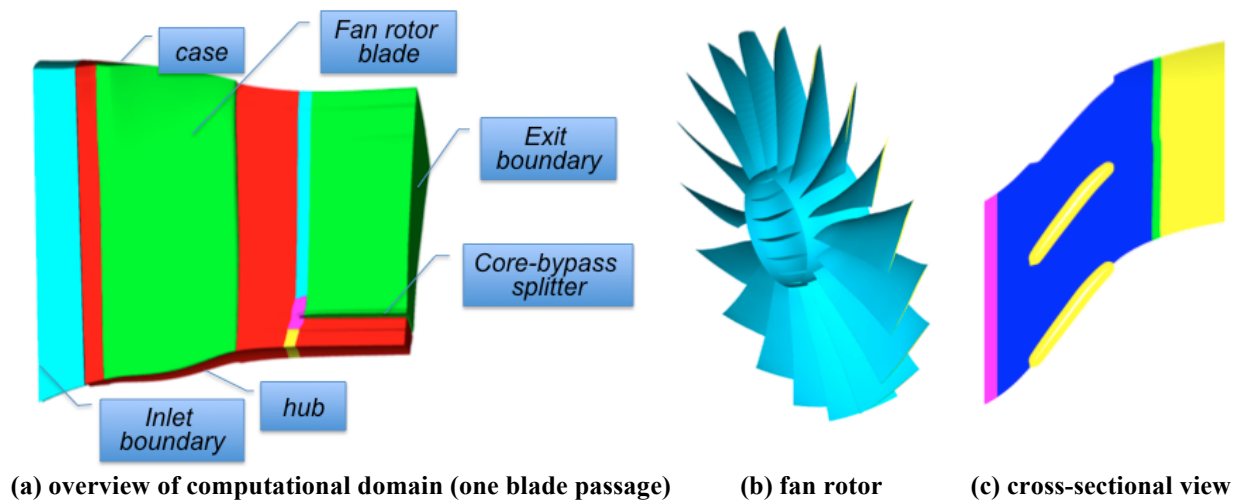


Figure 1. Computational domain used in fan aerodynamic analysis.

Initial analysis is carried out with clean inflow prescribed at the inlet boundary. This condition represents typical operation at cruise conditions for a fan operating *without* boundary layer ingestion. For example, an engine in a typical under-wing mount would experience clean inflow if no crosswind were present. The inlet profile has only radial variations of total pressure, total temperature, radial flow angle, and tangential flow angle. One blade passage is used for the computations and periodic boundary conditions are imposed in the circumferential direction based on an assumed symmetry of the flowfield in each blade passage. A converged solution is obtained for a prescribed exit boundary condition and the speedline is obtained by varying the exit boundary condition, keeping the rotational speed fixed. Figure 2 shows the performance characteristics of the fan, adiabatic efficiency and total pressure ratio, for the design speed. No specific attempt is made to locate the stall boundary, rather the results shown Fig. 2 are those for which fully converged flowfields were obtained. The performance characteristics with clean inflow serve as a baseline for the following computations with distorted inflow.

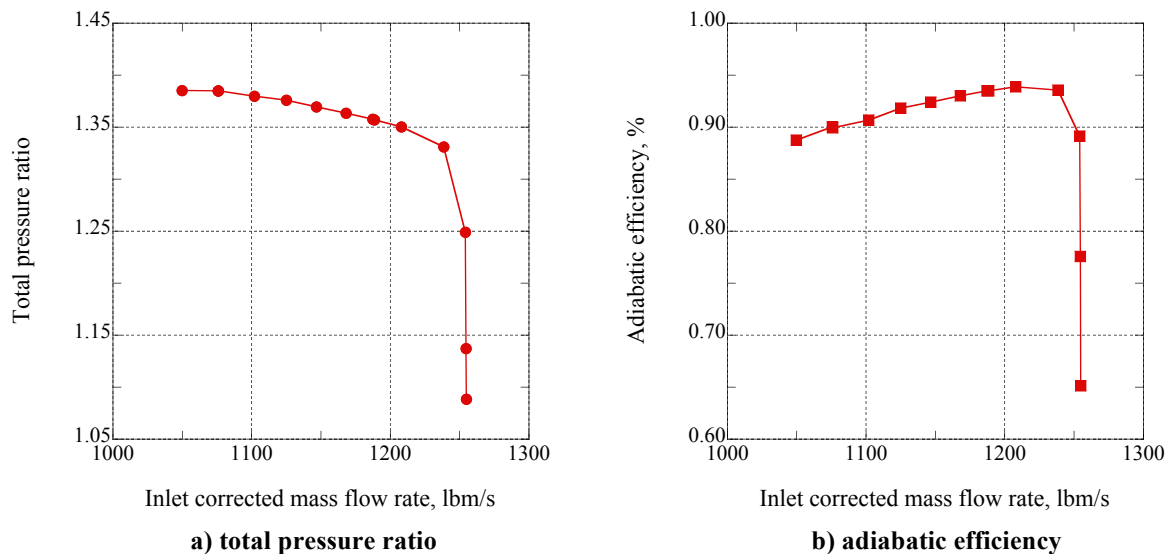


Figure 2. Performance characteristics of fan with clean inflow.

As mentioned previously, an optimization-based parametric inlet design process⁸ was used to design the inlet with reduced inlet total pressure loss and reduced distortion harmonic amplitudes as compared to the NASA Inlet A. The inlet flowfield is not part of the current computations. Instead, the flowfield from an intermediate inlet design iteration, identified as UTRC P3 inlet in Ref. 8, provides the inlet boundary condition for the fan computations. Due to the shape of the inlet, this flowfield is not axisymmetric. Rather, it contains both radial and circumferential variations in flow quantities. The relevant flow quantities required to fully prescribe the inlet boundary condition for the fan computational domain are shown in Fig. 3. Note that for this computation of the 18-bladed fan, all 18 blade passages are included in the computational domain. The time-domain computations are advanced with 100 time steps per passage, or 1800 time steps per rotor revolution; the solution is converged to periodicity after 6 revolutions. Figure 4 shows the variation of the instantaneous total pressure ratio for various blade passages as these passages traverse the inlet distortion. The repeating variation for any particular passage indicates the periodicity of the flowfield in time, and the shift of the results along the time axis for different passages indicates that each passage has the same flowfield when it is at a particular circumferential location at different times. The instantaneous average value over 18 passages is also shown for comparison.

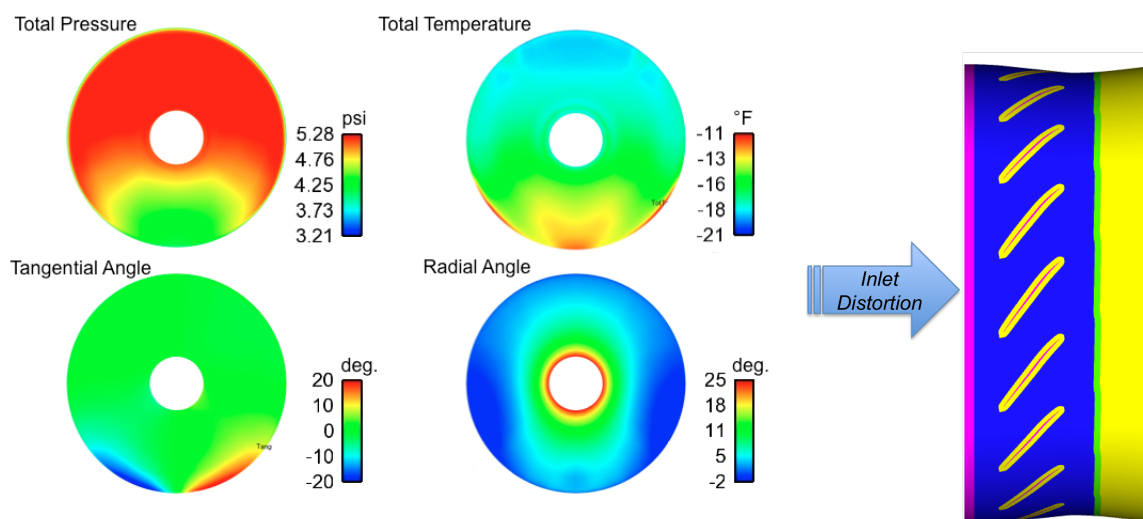


Figure 3. Inlet boundary conditions for fan computational domain.

Figure 5 shows the variation of the total pressure ratio for different passages as a function of the mass flow rate through each passage. The instantaneous average value over 18 passages is also shown for comparison. The overlay of the values for two revolutions and for different passages indicates once again the periodicity in time and across the passages. The excursion of the instantaneous value also provides an indication of the variation in the flowfield in each passage as it traverses the inlet distortion. Note that the mass flow rate values in Fig. 5 are for each nominal passage as opposed to the values for the full rotor in Fig. 2. Also, note that a simplified approximation is used to calculate the instantaneous pressure ratio and mass flow rate in each blade passage using the grid block in place of computed stream tubes.

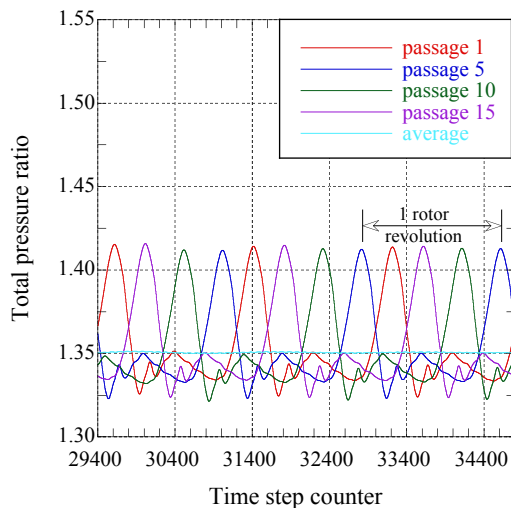


Figure 4. Periodicity of the rotor flowfield.

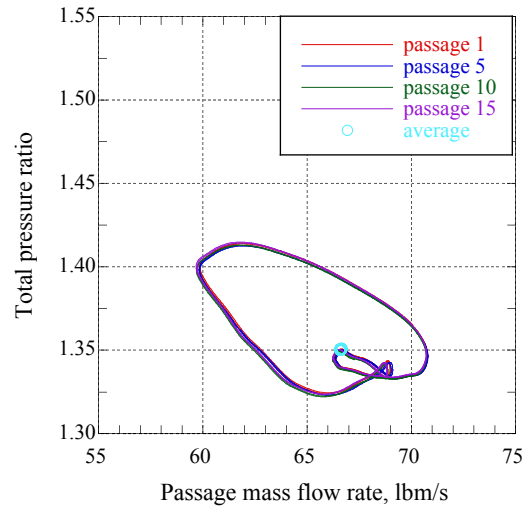


Figure 5. Variation of performance due to inlet distortion.

III. Fan Blade Structural Analysis

The aerodynamic design iteration of the BLI fan is used to create a structural model. It is assumed that the blades are made of Titanium alloy Ti-6Al-4V, which is typically used for scale model fan blades. In the structural model, 8-node hexahedral or brick elements are used and the blade root section is fully constrained in the analysis (no blade attachment is modeled). In addition to the centrifugal loads, nominal pressure load is prescribed. Nonlinear static and modal analyses are performed using commercial finite element analysis software to calculate the blade static deflection, static stress, and modal deflections (mode shapes), stresses, and frequencies. The analyses include the effects of centrifugal stiffening and softening. The mode shape and frequency results for the first four modes are shown in Fig. 6. It can be noted that the first mode is predominantly bending and the third mode is predominantly torsion; these two modes are considered for the flutter stability analysis in a following section.

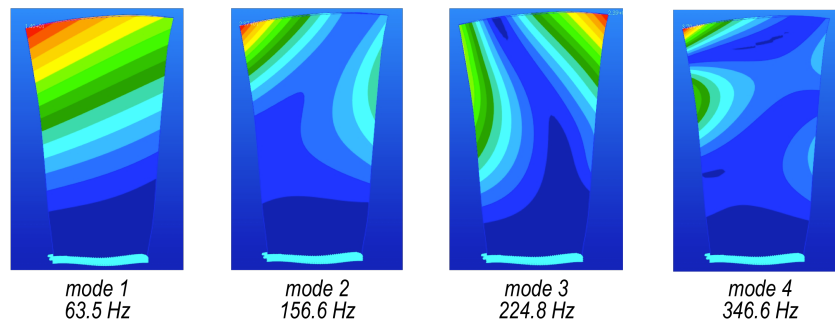


Figure 6. Fan blade vibration mode shapes and frequencies at design speed.

IV. Fan Blade Forced Vibration Response

The blade structural dynamics can be described in modal form by the following equation:

$$[M]\{\ddot{q}\} + [K]\{q\} = \{AD\} \quad (1)$$

where $[M]$ is the modal mass matrix, $[K]$ is the modal stiffness matrix, $\{q\}$ is the generalized displacement vector, $\{AD\}$ is the motion-independent aerodynamic load vector that is referred in this context as the modal force vector, and the overdot denotes time derivative. Note that damping is not included, which is expected to provide conservative results.

For a frequency of excitation ω , the generalized displacement vector of an undamped blade can be written as:

$$\{q\} = \left[[K] - \omega^2 [M] \right]^{-1} \{AD\} \quad (2)$$

The components of modal force can be defined by the following equation:

$$AD_n = \int \bar{\delta}_n \cdot p d\bar{A} \quad (3)$$

where $\bar{\delta}$ is the modal displacement vector, p is the aerodynamic pressure, \bar{A} is the blade surface area vector, and the subscript n denotes the mode index.

The inlet distortion provides a periodic excitation for each blade with a fundamental period of one rotor revolution. The unsteady pressure from the unsteady flowfield computed by TURBO is used with the blade modal displacement and area to calculate the modal force. Figure 7 shows this time variation of modal force for the first four modes. Since the flowfield has converged to periodicity, the modal force is seen in Fig. 7 as a periodic function of time. Figure 8 shows the Fourier components of modal force. The first and second harmonics are significant in magnitude, with a rapid drop-off beyond the fourth harmonic. However, it can be noted from Eq. (2) that the forced response vibration amplitude will be large if the excitation frequency is nearly equal to the natural frequency. To determine conditions at which the excitation frequency is nearly equal to the natural frequency, a Campbell diagram is constructed by repeating the modal analysis at different rotational speeds. Figure 9 shows the Campbell diagram for the fan rotor blade. The rotational speed is non-dimensionalized by the design value. The lines of constant slope are the “engine order (EO)” excitation lines that correspond to the harmonic content of the excitation. For example, the third harmonic in Fig. 8 acts as a 3 EO excitation that has a frequency nearly equal to the mode 2 frequency at design rotational speed (highlighted with a circle on Fig. 9). Similarly, the 7 EO excitation frequency is nearly equal to the mode 4 frequency.

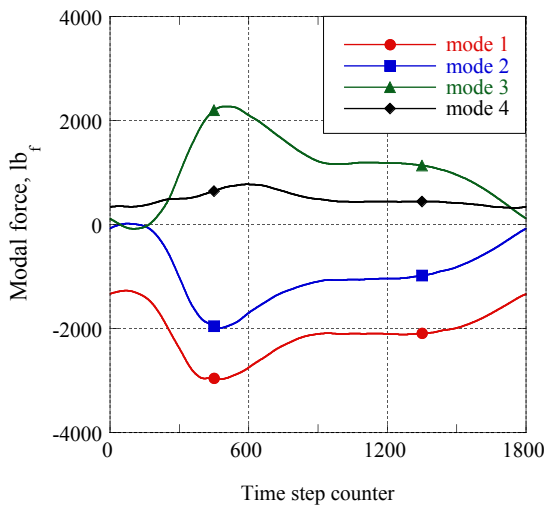


Figure 7. Modal force variation.

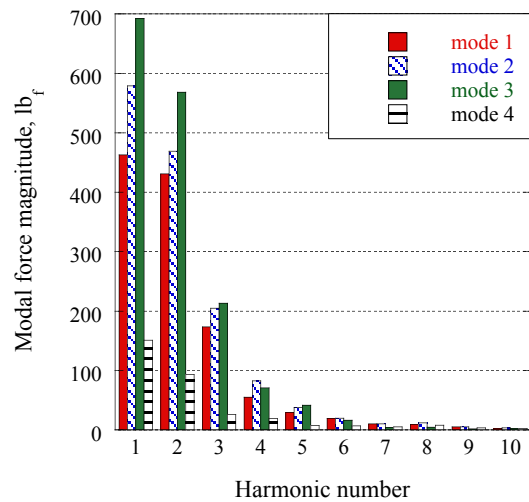


Figure 8. Fourier components of modal force.

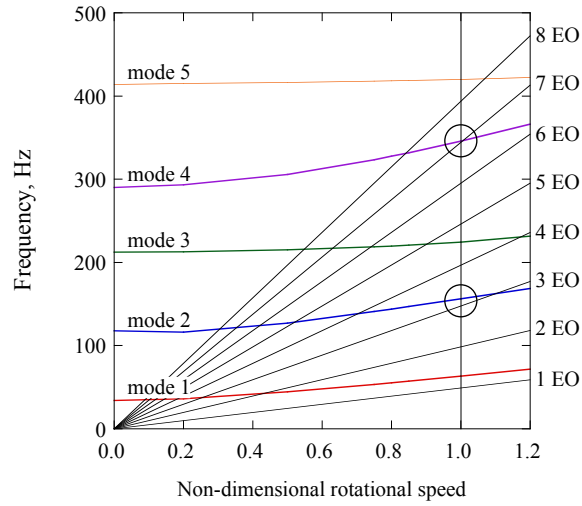


Figure 9. Campbell diagram for BLI fan blade.

The forced vibration response or dynamic stress at design speed can be calculated to include contributions from various modes for any given engine order excitation. Rewriting Eq. (2) for each harmonic (engine order), the generalized displacement for n^{th} mode due to r^{th} harmonic excitation can be written as:

$$\{q_{nr}\} = \left[[K_n] - \omega_r^2 [M_n] \right]^{-1} \{AD_{nr}\} \quad (4)$$

Then, the blade displacements u_r resulting from the r^{th} harmonic excitation are given by:

$$u_r = \sum_n \phi_n q_{nr} \quad (5)$$

where ϕ_n is the n^{th} mode shape. Similarly, the dynamic stress response amplitudes σ_r for the r^{th} harmonic excitation can be obtained from the modal stress s_n as:

$$\sigma_r = \sum_n s_n q_{nr} \quad (6)$$

The results of such calculations are shown in Fig. 10 and Table 1. Four modes are included in the analysis corresponding to eight engine order excitations. Figure 10 shows the increased generalized displacement in mode 2 for engine order 3 excitation (q_{23}), resulting from an excitation frequency close to the natural frequency (as seen in Fig. 9). Also, Table 1 shows the resulting increased dynamic stress from engine order 3 excitation. Similarly, the small frequency margin for mode 4 and engine order 7 (Fig. 9) is seen to result in an increased dynamic stress from engine order 7 excitation (Table 1). Note that the stress values listed in Table 1 are the von Mises stresses. Also, note that the analysis was done for the design rotational speed. It is expected that the on-resonance analysis near the design speed will result in significantly higher dynamic stresses. Work is in progress to perform this on-resonance analysis.

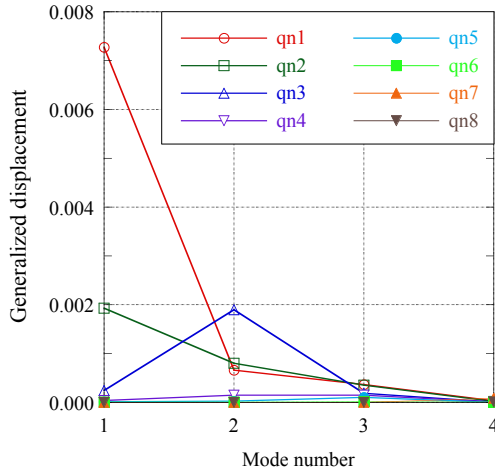


Figure 10. Fan blade forced vibration response.

Table 1. Vibration amplitude and dynamic stress for different engine order excitations at design speed.

Harmonic or engine order	Vibration amplitude (at tip trailing edge), inch	Dynamic stress amplitude (at root of blade), psi
1	5.5×10^{-2}	273
2	3.0×10^{-2}	290
3	1.9×10^{-2}	666
4	3.1×10^{-3}	308
5	2.6×10^{-3}	169
6	2.7×10^{-4}	33
7	7.0×10^{-4}	427
8	6.0×10^{-5}	19

V. Fan Blade Flutter Stability

The flutter stability of the fan is evaluated using the TURBO aeroelastic analysis code. The energy method²¹ or work-per-cycle approach is used to calculate aerodynamic damping to determine flutter stability as described in Ref. 22. For a clean inflow prescribed at the inlet boundary, the flowfield through the blade row is first calculated with no prescribed blade vibration. Starting with this converged steady flowfield, blade vibrations are prescribed in a selected mode, frequency, and nodal diameter pattern or phase angle. Note that the number of different possible nodal diameter patterns is equal to the number of blades that are on the fan rotor. After the transients in the flowfield decay, and a periodic flowfield is obtained, the work done on the vibrating blade is calculated for a cycle of blade vibration as follows:

$$W = \oint_{\text{surface}} -p d\vec{A} \cdot (\partial \vec{X} / \partial t) dt \quad (7)$$

where, p is the aerodynamic pressure due to blade vibration, A is the blade surface area vector, \vec{X} is the displacement vector on the blade surface, and t denotes time. The aerodynamic damping ratio (ζ) can be approximately related to the work-per-cycle (W) and the average kinetic energy (K_E) of the blade over one cycle of vibration through the following expression:

$$\zeta \approx -W / 8\pi K_E \quad (8)$$

If aerodynamic damping is negative, flutter can occur. Note that the structural damping (material and mechanical damping) has not been considered.

A. Clean Inflow

Initial fan flutter calculations are performed at design operating speed near peak efficiency condition with clean inflow prescribed at the inlet boundary. The computational domain consisted of all 18 blade passages (full rotor analysis). Figure 11 shows the results of the calculations with all blades vibrating in-phase (0 nodal diameter) in mode 1 (bending). Individual blade values are shown to converge to the average value within 10 cycles of vibration. The converged value is positive indicating no flutter at the condition analyzed. Similar calculations are performed with vibrations in other nodal diameter patterns (different interblade phase angles). The converged results are summarized in Fig. 12. It can be noted that aerodynamic damping has a fairly large range of variation with nodal diameter pattern, with low values for low nodal diameter patterns. For all nodal diameter patterns considered, aerodynamic damping is positive, indicating no flutter for the conditions analyzed, namely, design operating speed near peak efficiency condition. Since decreasing mass flow rate along the speedline (moving towards stall) can sometimes result in reduced aerodynamic damping and possibly flutter, calculations are performed at the design

operating speed near stall condition (approximately 11% lower mass flow rate). Only results for the selected range of nodal diameter patterns are shown in Fig. 13. The lowest aerodynamic damping value is seen to decrease as the operating point is changed from near peak efficiency to near stall. For mode 1 (bending) vibrations, aerodynamic damping reaches low values for the 1 nodal diameter pattern, although all calculated values remain positive.

Figure 14 shows the results of calculations performed for mode 3 (torsion) at design operating speed near peak efficiency condition with clean inflow. In contrast to mode 1, the aerodynamic damping stays within a narrow range of values. All calculated aerodynamic damping values are positive, indicating no flutter for the conditions analyzed; minimum values are higher for mode 3 as compared to mode 1. Calculations are also performed at the design operating speed near stall condition for a selected range of nodal diameter patterns. No significant change in aerodynamic damping is observed as the operating point is changed from near peak efficiency to near stall.

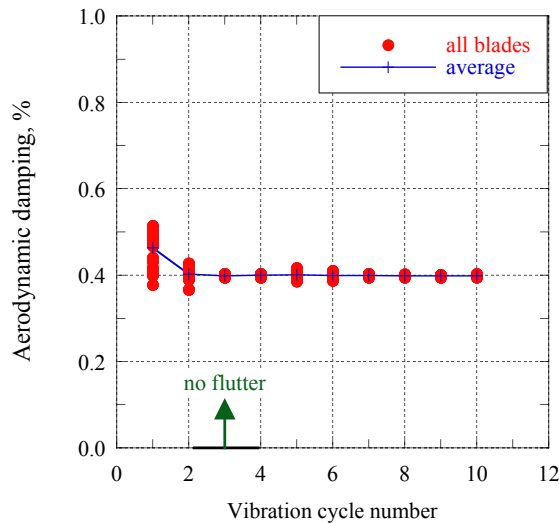


Figure 11. Aerodynamic damping with clean inflow at design operating speed, near peak efficiency condition, mode 1 vibration, 0 nodal diameter pattern

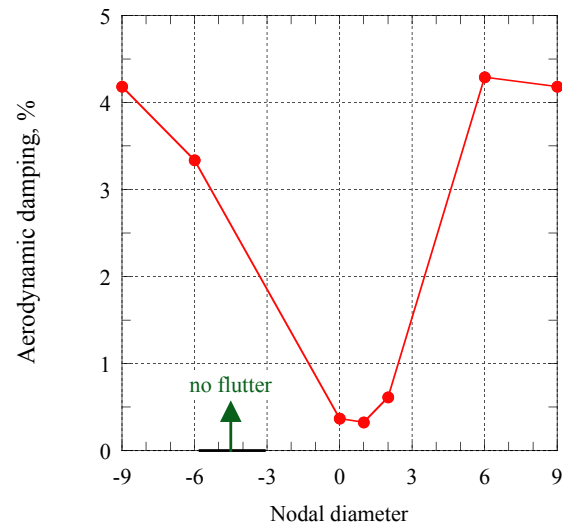


Figure 12. Aerodynamic damping with clean inflow at design operating speed, near peak efficiency condition, mode 1 vibration, various nodal diameter patterns

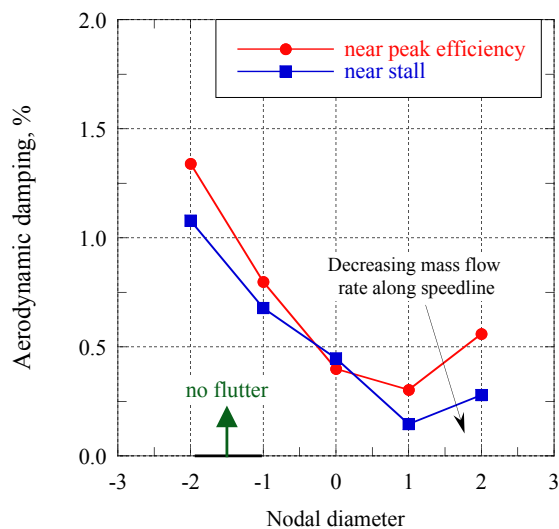


Figure 13. Effect of operating point on aerodynamic damping with clean inflow at design operating speed, mode 1 vibration, various nodal diameter patterns

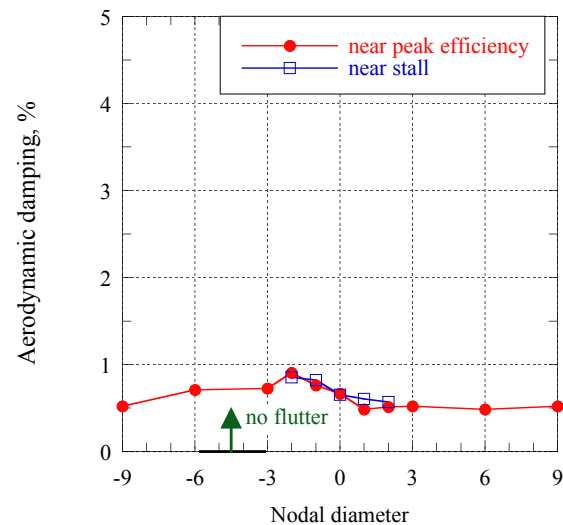


Figure 14. Aerodynamic damping with clean inflow at design operating speed, near peak efficiency condition, mode 3 vibration, various nodal diameter patterns

B. Distorted Inflow

Typically, in a linear formulation fan flutter stability and forced response due to aerodynamic excitations are considered separately. Moreover, fan inlet distortion is typically considered only in the context of cross-wind operation at low forward speed operation on the ground. In the present case of the BLI fan, the concern is that the inlet distortion is persistent at all operating conditions and includes multiple harmonics. Previous studies²³⁻²⁵ have indicated that nonlinear interactions between inlet distortion and blade vibrations may be important. The influence of inlet distortion on flutter stability is related, in part, to the changes in operating conditions of individual blades as they move through the distorted inlet flow as can be seen in Fig. 5. In addition, since the fan blade rotational frequency is typically not an integral multiple of the blade vibration frequency, each blade vibration cycle takes place in a different flowfield depending on the location of the blades relative to the inlet distortion.

Various approaches are considered to evaluate flutter stability with distorted inflow: (i) circumferentially average the distorted inflow to obtain an equivalent radial profile and use work-per-cycle analysis, (ii) select a portion of the inlet distortion to represent a “worst-case” inflow condition that is used at all circumferential locations and use work-per-cycle analysis, (iii) prescribe blade vibrations and distorted inflow simultaneously, use work-per-cycle analysis, average the results over all blades, and over multiple blade vibration cycles, (iv) use tightly-coupled aeroelastic analysis with distorted inflow; blade vibrations are determined as part of the computations; post-process time history to estimate average damping over all blades and multiple vibration cycles. Upon considering the above approaches, approach (iii) is selected as the preferred approach that would avoid having to make large changes to the computational code, not be overly conservative, and not average out the effects of the inlet distortion entirely. It is recognized that due to the varying upstream conditions, each vibration cycle of each fan blade will be unique, and thus there will not be a convergence to a single value for all blades after running multiple vibration cycles. Instead, one would expect to obtain results that represent a range of aerodynamic damping values.

Figure 15 shows the calculated aerodynamic damping with distorted inflow for design operating speed, near peak efficiency condition, mode 1 vibration, and 0 nodal diameter pattern. The results for individual blades are plotted, along with the average over all the blades. Since the period of blade vibration is not the same as the period of blade rotation, each vibration cycle for each blade occurs in a different flowfield, resulting in a different aerodynamic damping. This plot shows a variation of less than 0.3% in aerodynamic damping for different blades resulting from the circumferential variations in the flowfield due to the distorted inflow. The average over all blades is nearly unchanged after the first vibration cycle. Figure 16 shows the same results plotted as a variation with blade number; the average over all vibration cycles is seen to be nearly the same for all blades. Figure 17 shows a comparison of calculated average aerodynamic damping for clean and distorted inflow; this comparison is for design operating speed, near peak efficiency condition, mode 1 vibration, and 0 nodal diameter pattern. The results for the distorted inflow are slightly lower, which may be possibly due to a slightly different mean operating condition.

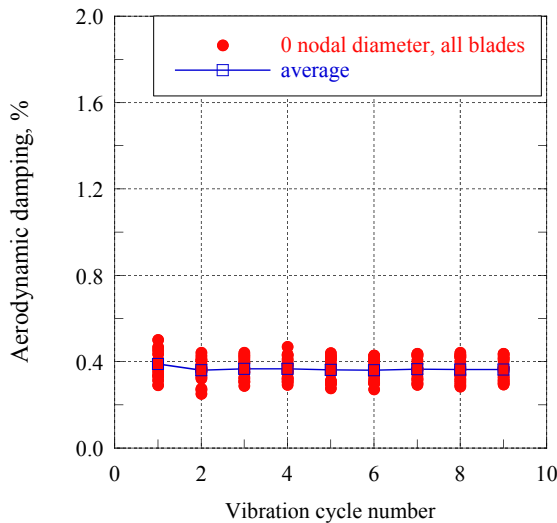


Figure 15. Aerodynamic damping with distorted inflow at design operating speed, mode 1 vibration, 0 nodal diameter pattern

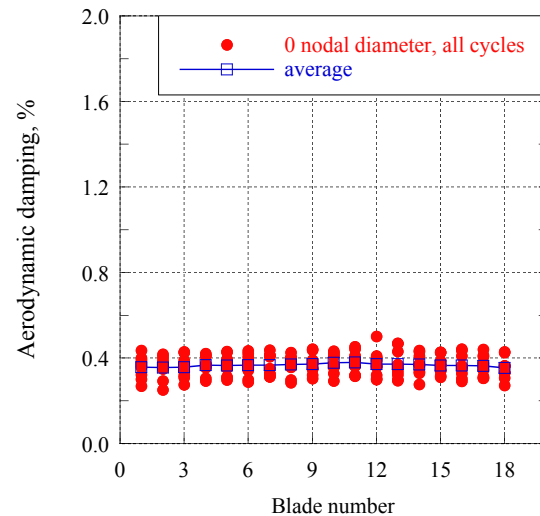


Figure 16. Aerodynamic damping for all blades with distorted inflow at design operating speed, mode 1 vibration, 0 nodal diameter pattern

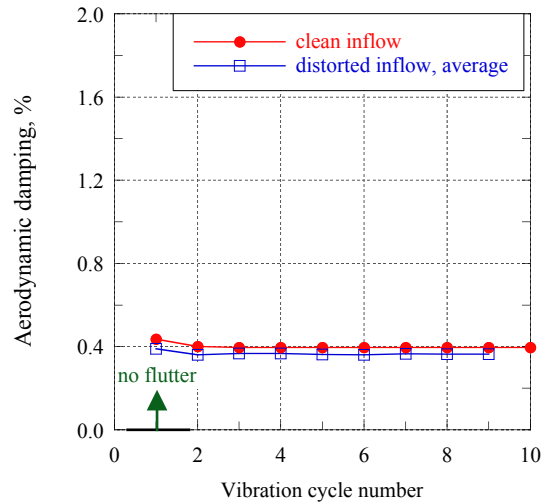


Figure 17. Aerodynamic damping at design operating speed, mode 1 vibration, 0 nodal diameter pattern with clean and distorted inflow

Figure 18 and 19 show the calculated aerodynamic damping with distorted inflow for design operating speed, near peak efficiency condition, mode 1 vibration, and 1 nodal diameter pattern. These results are of particular interest since the 1 nodal diameter pattern showed the lowest aerodynamic damping for clean inflow (Fig. 13). Figure 18 shows that the range of variation in aerodynamic damping over all blades is approximately 0.3%, which is slightly larger than the range for 0 nodal diameter. The average value is nearly unchanged after the first vibration cycle. Figure 19 shows a slightly higher variation in average aerodynamic damping with blade number as compared to the 0 nodal diameter results (Fig. 16), nonetheless this variation of the average value is quite small. As compared to the 0 nodal diameter pattern, these results show lower average values of aerodynamic damping. The differences between the average values for clean inflow and distorted inflow are quite small and all calculated values of aerodynamic damping are positive.

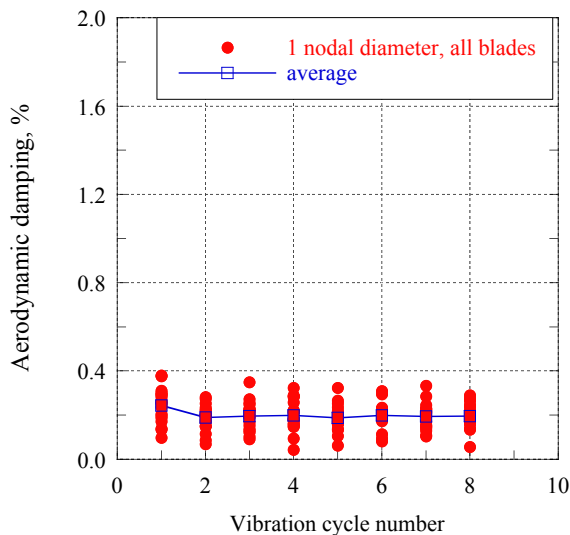


Figure 18. Aerodynamic damping with distorted inflow at design operating speed, mode 1 vibration, 1 nodal diameter pattern

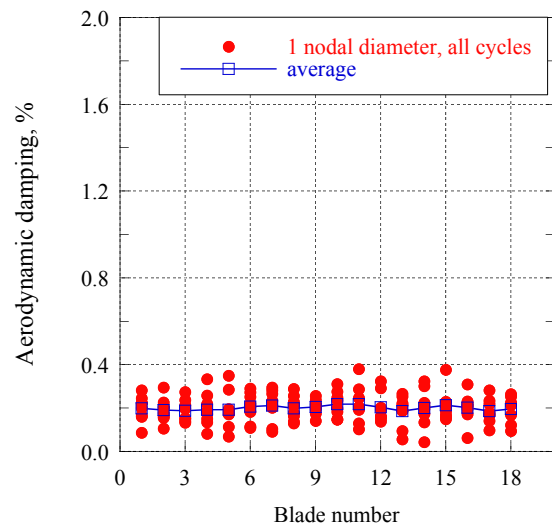


Figure 19. Aerodynamic damping for all blades with distorted inflow at design operating speed, mode 1 vibration, 1 nodal diameter pattern

VI. Concluding Remarks

To realize the benefits of Boundary Layer Ingestion (BLI) propulsion, the fan must have acceptable aeromechanical characteristics to operate in the persistent inlet distortion created by the BLI inlet. In this study, an intermediate design of a fan operating with a BLI inlet has been analyzed for its aeromechanical characteristics in the presence of distorted in-flow. The inlet duct was not modeled as part of this study. Instead, the inlet distortion from a separate flow calculation was imposed as the inlet boundary condition for the fan analysis.

A structural model was created to analyze the structural dynamics characteristics of the fan, and a Campbell diagram was constructed. The forced response analysis provided the dynamic stresses at design rotational speed. Further analysis is required to examine the forced response at other rotational speeds where the engine order excitation frequency coincides with a blade natural frequency (on-resonance conditions). Further work is also needed to understand the effects of blade root fixity modeling on blade natural frequencies and mode shapes.

Baseline fan flutter analysis was performed at design speed using clean inflow conditions. The aerodynamic damping near peak efficiency condition, calculated using the energy method, was seen to have low values for low nodal diameters for the first structural mode. For operating conditions near stall, the aerodynamic damping was seen to drop to very low values. However, none of the results showed negative aerodynamic damping that would indicate flutter. Similar analysis of the third mode also showed no flutter at design speed, both near peak efficiency and stall conditions. Further analysis is required at off-design conditions where flutter is more frequently encountered. Also, additional analysis is required to understand the sensitivity of the flutter stability results to physical and numerical parameters.

Different approaches were considered to analyze flutter stability in the presence of the BLI distortion. Analysis was performed with both the inlet distortion and blade vibrations simultaneously modeled. No flutter was encountered in the limited number of cases examined for the first vibration mode. To reduce the possibility of aeromechanical difficulties during the operation of the BLI fan, many possible combinations of rotational speed, operating condition, vibration mode, and nodal diameter pattern need to be analyzed for flutter stability.

Current aeromechanical analyses of the intermediate design of the BLI fan have not shown any problems of flutter or forced response. The analyses completed thus far represent initial work towards risk reduction in the design and testing of the BLI fan. Future work will focus on completing the analysis for this intermediate design and performing similar analyses for the final design that will be tested in the wind tunnel. Additional follow-on work in the future may be related to coupled inlet-fan analyses, which would model with greater accuracy the operation of this BLI fan. Further, a tightly coupled aeroelastic analysis may be considered in the future to provide more detailed and accurate representation of the interactions between blade vibrations and inlet distortion.

Acknowledgments

The work described in this paper was performed at NASA Glenn Research Center (GRC) in collaboration with United Technologies Research Center (UTRC). The authors would like to thank Mr. David Arend (NASA GRC Team Lead, Robust Design of Embedded Engine Systems) and Dr. Gregory Tillman (UTRC Team Lead). The authors are grateful for the support of this work provided by the Subsonic Fixed Wing Project (Dr. Rubén Del Rosario, Project Manager; Dr. Michael Hathaway, Technical Challenge Lead), and the Environmentally Responsible Aviation Project (Dr. Fayette Collier, Project Manager; Dr. Kenneth Suder, Propulsion Sub-project Manager).

References

- ¹Smith, L. H., "Wake Ingestion Propulsion Benefit," *AIAA Journal of Propulsion and Power*, Vol. 9, No. 1, Jan.-Feb., 1993, pp. 74-82.
- ²Daggett, D., Kawai, R., and Friedman, D., "Blended Wing Body Systems Studies: Boundary Layer Ingestion Inlets with Active Flow Control," NASA/CR-2003-212670, December 2003.
- ³Kawai, R., Friedman, D., and Serrano, L., "Blended Wing Body (BWB) Boundary Layer Ingestion (BLI) Inlet Configuration and Systems Studies," NASA/CR-2006-214534, December 2006.
- ⁴Plas, A. P., "Performance of a Boundary Layer Ingesting (BLI) Propulsion System, AIAA-2007-450, January 2007.
- ⁵Nickol, C. L., "Silent Aircraft Initiative Concept Risk Assessment," NASA/TM-2008-215112, February 2008.
- ⁶Nickol, C. L., and McCullers, L. A., "Hybrid Wing Body Configuration System Studies," AIAA-2009-931, January 2009.
- ⁷Tillman, T. G., Hardin, L. W., Moffitt, B. A., Sharma, O. P., Lord, W. K., Berton, J., and Arend, D., "System-Level Benefits of Boundary Layer Ingesting Propulsion," invited presentation, AIAA 49th Aerospace Sciences Meeting, January 2011.
- ⁸Florea, R. V., Matalanis, C., Hardin, L. W., Stucky, M., and Shabbir, A., "Parametric Analysis and Design for Embedded Engine Inlets," AIAA 48th AIAA/ASME/SAE/ASEE Joint Propulsion Conference & Exhibit, Jul 30- Aug 1, 2012.
- ⁹Berrier, B. L., Carter, M. B., and Allan, B. G., "High Reynolds Number Investigation of a Flush-Mounted, S-Duct Inlet with Large Amounts of Boundary Layer Ingestion," NASA/TP-2005-213766, 2005.

- ¹⁰Chen, J.-P., and Whitfield, D. L., "Navier-Stokes Calculations for the Unsteady Flowfield of Turbomachinery," AIAA Paper 1990-0676, January 1990.
- ¹¹Chen, J.-P. and Briley, W. R., "A Parallel Flow Solver for Unsteady Multiple Blade Row Turbomachinery Simulations," ASME Paper GT2001-0348, June 2001.
- ¹²Srivastava, R., Bakhle, M. A., and Keith, T. G., Jr., "Numerical Simulation of Aerodynamic Damping for Flutter Analysis of Turbomachinery Blade Rows," *AIAA Journal of Propulsion and Power*, Vol. 19, No. 2, March 2003.
- ¹³Srivastava, R., Bakhle, M. A., Keith, T. G., Jr., and Stefko, G. L., "Flutter Analysis of a Transonic Fan," ASME Paper GT-2002-30319, June 2002.
- ¹⁴Bakhle, M. A., Liu, Jong S., Panovsky, Josef, Keith, Theo G. Jr., and Mehmed, Oral, "Calculation and Correlation of the Unsteady Flowfield in a High Pressure Turbine," ASME Paper GT-2002-30322, June 2002.
- ¹⁵Panovsky, Josef, James, Darrell K., and Hassan, Khaled K., "An Assessment of Fan Flutter Using TURBO," 5th National Turbine Engine High Cycle Fatigue Conference, published by Universal Technology Corporation, Dayton, Ohio, April 2000.
- ¹⁶Panovsky, J., Liu, J. S. and Bakhle, M. A., "Comparisons of Experimental and Computational Forced Response in a High Pressure Turbine", Proceedings of the 7th National Turbine High Cycle Fatigue Conference, published by Universal Technology Corporation, Dayton, Ohio, April 2002.
- ¹⁷Kielb, Robert E., Barter, John W., Thomas, Jeffrey P., and Hall, Kenneth C., "Blade Excitation by Aerodynamic Instabilities," ASME Paper GT2003-38634, June 2003.
- ¹⁸Sanders, A. J., Hassan, K. K. and Rabe, D. C., "Experimental and Numerical Study of Stall Flutter in a Transonic Low-Aspect Ratio Fan Blisk," *ASME Journal of Turbomachinery*, Vol. 126, No. 1, pp. 166-174, January 2004.
- ¹⁹Sanders, A. J., "Stall Flutter Assessment of and Advanced Design Transonic Fan Using TURBO-AE", Proceedings of the 6th National Turbine High Cycle Fatigue Conference, published by Universal Technology Corporation, Dayton, Ohio, April 2001.
- ²⁰Herrick, G. P., "Effects of Inlet Distortion on Aeromechanical Stability of a Forward-Swept High-Speed Fan," AIAA Paper 2010-6711, August 2010.
- ²¹Carta, F. O., "Coupled Blade-Disk-Shroud Flutter Instabilities in Turbojet Engine Rotors," *Trans ASME Journal of Engineering for Power*, Vol. 89, No.3, pp. 419- 426, July 1967.
- ²²Bakhle, M. A., Reddy, T. S. R., and Stefko, G. L., "Comparisons of Flutter Analyses for an Experimental Fan," NASA/TM-2010-216221, Apr. 2010.
- ²³Li, H. D., and He, L., "Single-Passage Analysis of Unsteady Flows Around Vibrating Blades of a Transonic Fan Under Inlet Distortion," *ASME Journal of Turbomachinery*, Vol. 124, No. 2, pp. 285-292, April 2002.
- ²⁴Ekici, K., and Hall, K. C., "Nonlinear Frequency-Domain Analysis of Unsteady Flows in Turbomachinery with Multiple Excitation Frequencies," *AIAA Journal*, Vol. 46, No. 8, pp. 1912-1920, August 2008.
- ²⁵Vahdati, M., Sayma, A. I., Bréard, C., and Imregun, M., "Computational study of intake duct effects on fan flutter stability," *AIAA Journal*, Vol. 40, No. 3, pp. 408-418, March 2002.